A Volcanological Paradox in a Thin-Section: Large Explosive Eruptions of High-Mg Magmas Explained Through a Vein of Silicate Glass in a Serpentinized Peridotite Xenolith (Hyblean Area, Sicily)

Alessandra Correale [1], **Vittorio Scribano** [2,*] and **Antonio Paonita** [1]

[1] Istituto Nazionale di Geofisica e Vulcanologia, Sezione di Palermo, Via Ugo La Malfa, 153, 90146 Palermo, Italy; alessandra.correale@ingv.it (A.C.); antonio.paonita@ingv.it (A.P.)

[2] Dipartimento di Scienze Biologiche, Geologiche e Ambientali, Università di Catania, Corso Italia 55, 95129 Catania, Italy

[*] Correspondence: scribano@unict.it

check for updates

Abstract: Ultramafic magmas (MgO $\geq$ 18 wt%) are generally thought to be primary mantle melts formed at temperatures in excess of 1600 °C. Volatile contents are expected to be low, and accordingly, high-Mg magmas generally do not yield large explosive eruptions. However, there are important exceptions to low explosivity that require an explanation. Here we show that hydrous (hence, potentially explosive) ultramafic magmas can also form at crustal depths at temperatures even lower than 1000 °C. Such a conclusion arose from the study of a silicate glass vein, ~1 mm in thickness, cross-cutting a mantle-derived harzburgite xenolith from the Valle Guffari nephelinite diatreme (Hyblean area, Sicily). The glass vein postdates a number of serpentine veins already existing in the host harzburgite, thus reasonably excluding that the melt infiltrated in the rock at mantle depths. The glass is highly porous at the sub-micron scale, it also bears vesicles filled by secondary minerals. The distribution of some major elements corresponds to a meimechite composition (MgO = 20.35 wt%; $Na_2O + K_2O < 1$ wt%; and $TiO_2 > 1$ wt%). On the other hand, trace element distribution in the vein glass nearly matches the nephelinite juvenile clasts in the xenolith-bearing tuff-breccia. These data strongly support the hypothesis that an upwelling nephelinite melt (MgO = 7–9 wt%; $1100 \leq T \leq 1250$ °C) intersected fractured serpentinites (T $\leq$ 500 °C) buried in the aged oceanic crust. The consequent dehydroxilization of the serpentine minerals gave rise to a supercritical aqueous fluid, bearing finely dispersed, hydrated cationic complexes such as $[Mg^{2+}(H_2O)_n]$. The high-Mg, hydrothermal solution "flushed" into the nephelinite magma producing an ultramafic, hydrous (hence, potentially explosive), hybrid magma. This hypothesis explains the volcanological paradox of large explosive eruptions produced by ultramafic magmas.

Keywords: Peridotite; silicate glass; serpentinite; meimechite; picrite; explosive eruption

1. Introduction

High-Mg magmas generally do not yield explosive eruptions with a volcanic explosivity index (VEI) $\geq$ 4 [1]. Such evidence is consistent with the low viscosity of Mg-rich silicate melts, as Mg^{2+} is an effective network-modifying cation [2]. Thus, basic magmas give rise to open-conduit volcanoes with dominantly effusive activities associated with either mild strombolian explosions or more energetic fire fountain episodes [3]. Nevertheless, there are exceptions to the aforementioned paradigm. For instance, tephrostratigraphic investigations [4] on Mount Etna volcano (Sicily, central Mediterranean area) have led to the surprising conclusion that powerful explosive eruptions in recent millennia were due to

batches of relatively primitive (alkalibasaltic) magma [5,6]. Similarly, [7], reporting on the eruptive history of the Kilauea volcano, Hawai'i, highlighted that the highest MgO melts were erupted during explosive, not effusive, periods. Mount Etna is one of the few examples of active volcanoes in which the occurrence of sub-plinian and plinian basaltic eruptions are well-documented in recent times (e.g., [8]). Accordingly, the explosive dynamics of modern Mount Etna have been related to a deep supply of volatile-rich, high-Mg magmas [6]. Coltelli et al. [9], on the basis of a detailed study on pyroclastic deposits in the eastern flanks of Mt. Etna, reported on a sub-plinian explosion that occurred 3930 ± 60 BP (^{14}C age) and was fed by picritic magma. Coltelli et al. [9] remarked that the lack of accessory lithic clasts and fine particles, the high vesicularity and good sorting of the deposits, suggested a purely magmatic mechanism for the eruption, ruling out interactions with groundwater. Moreover, [9] highlighted that the considered Etnean eruption was the only example of a large explosive picritic eruption known worldwide. Apart from picrites, there are worldwide cases of highly explosive activities from ultrabasic magmas in the past geological times. Kimberlitic magmas (MgO > 25 wt%: e.g., [10]), for instance, typically produced large explosive eruptions, as easily deduced from the characteristics of their diatreme structures and related tuff-breccia deposits [10,11].

An exceptionally high content in volatiles (mostly H_2O and/or CO_2) is generally invoked to explain large explosions produced by Mg-rich magmas [12,13]. There are two different schools of thought to explain such a high abundance in volatiles in primitive magmas. The first, more popular, hypothesis considers a mantle origin for the volatiles, which results from the partial melting of mantle rocks affected by hydrous and/or carbonate metasomatism (e.g., [14]). During melting, volatiles behave as an incompatible element [15], hence they tend to partition into the melt. The second hypothesis suggests the crustal origin of the volatiles, which relates to the interaction of an original, volatile-poor, mafic magma with crustal rocks bearing abundant hydrous minerals (e.g., serpentinites). The breakdown of the hydrous minerals yields huge quantities of volatiles (mostly supercritical H_2O), which can flush into the melt [16,17]. Here, we provide information about this problem by the petrographic and geochemical study of a silicate glass vein in a partially serpentinized peridotite xenolith from the Valle Guffari tuff-breccia deposit (Sicily, Southern Italy), recalling the notion that the "very small" can be helpful to understand the "very large" [18]. Furthermore, our data may raise some queries on the general thought that ultramafic magmas derive from a high degree of partial melting of the mantle source at very high temperature [19–23].

2. Regional Geological Setting and Sample Site

The Hyblean Plateau (Sicily, southern Italy: Figure 1) consists of an uplifted, relatively un-deformed crustal section, Mesozoic to Cenozoic in age, of marine limestones, marls, and volcanic rocks that sits upon a buried pre-Triassic basement. This region is affected by a NNE-SSW and NE-SW trending fault system [24]. In the time interval from late Triassic to lower Pleistocene, intermittent, dominantly submarine, volcanic activity occurred in this area [25]. Highly altered pillow-fragment breccias and hyaloclastite lenses underlaying rudists-bearing carbonate horizons, Upper Cretaceous in age, crop out in the southernmost coastal area of the Plateau and sporadically along the Ionian coast. However, most of the Hyblean volcanic rocks, Neogene to Quaternary in age, are exposed in an area of about 350 km^2 in the central and northeastern parts of the Plateau. Basalts, with both tholeiitic (E-MOR-type) and alkaline (OI-type) affinity, are the most common volcanic rocks in this area, with minor nephelinites [25–31].
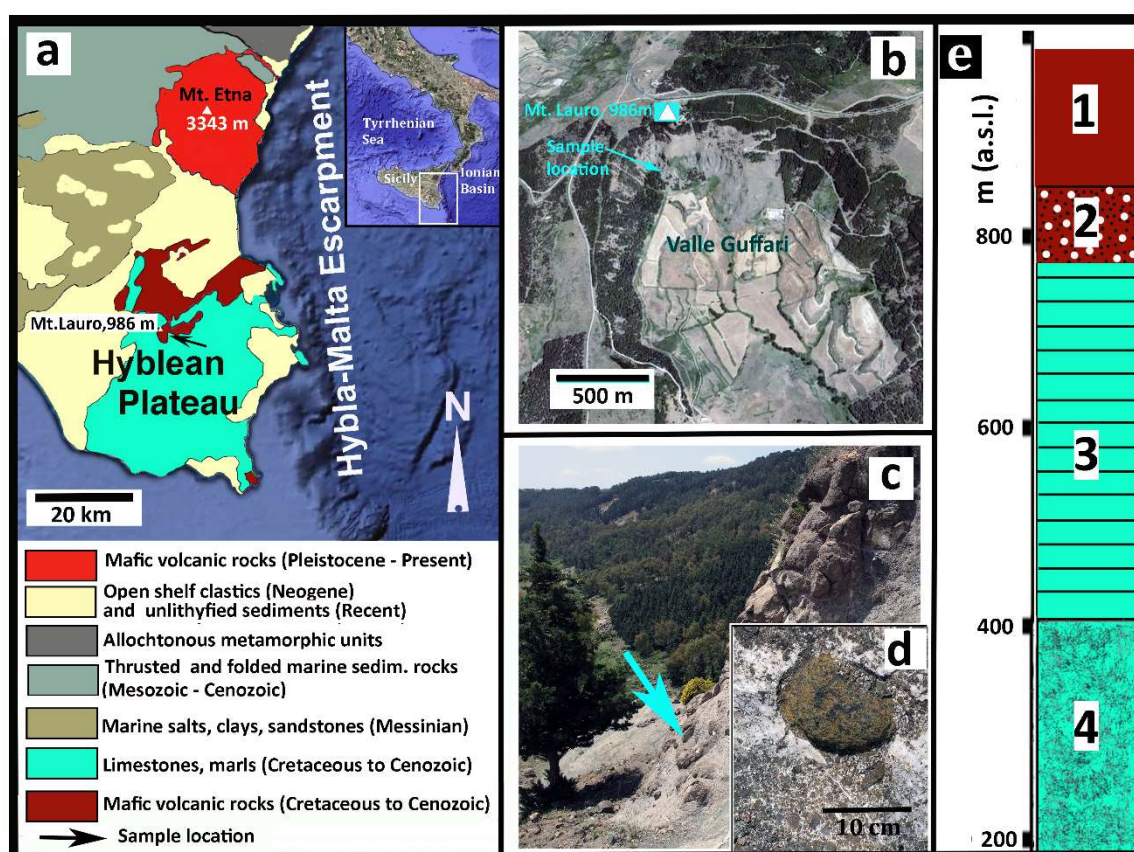
Figure 1. Synoptic geological description. (**a**) Geological sketch map of the eastern sector of Sicily. The arrow indicates the sample location. (**b**) Satellite view of Valle Guffari (From GoogleEarth) where additional information is indicated, as well the sample location. (**c**) Picture of the particular area of Valle Guffari where the sample was taken, as the arrow precisely indicates (37°06′36.24N; 14°49′24.39E). The lower box (**d**) shows a close view of the tuffsite-breccia with a typical peridotite xenolith, very similar to the sample. (**e**) Essential stratigraphy of the Valle Guffari area. Legend: Tholeiite basalts (Late Pliocene); 2. Xenolith-bearing nephelinitic tuff-breccia (Early Messinian); 3. Marls (Tellaro Formation, Tortonian); 4. Calcarenites and Marls (Langhian).

There are a few tuff-breccia deposits among the Hyblean volcanic formations, related to diatreme eruptions in shallow sea conditions, Upper Miocene in age [32]. Deep-seated xenoliths entrained in the diatremic tuff-breccia consist of mantle peridotites (spinel-facies harzburgite and rare lherzolite), pyroxenites, gabbroic rocks including sheared oxide-gabbros, and sedimentary lithologies.

The Hyblean xenoliths, particularly the sheared ferrogabbros, provide evidence of the oceanic affinity of the unexposed basement [33–37], although this is traditionally ascribed to the African (Nubian) continental plate [38–40]. The African plate hypothesis is chiefly based on the interpretation of seismic data, even though these data are either compatible with lower continental crust or serpentinized peridotites [41–43]. Moreover, the Africa continental model for the Hyblean Plateau (and the entire Central Mediterranean area) is supported by Precambrian granitoids recovered in a few core drills in the southern, cratonic part, of Tunisia, whereas in its central and northern parts, the pre-Triassic basement was never sampled [44]. More importantly, some authors provided inference on the oceanic nature of the northern Tunisian basement, albeit close to the southern Tethyan margin [45].

Even though the problem of the geodynamic setting of Sicily is outside the aims of this paper, it is important to highlight that geophysical and other geological data are compatible with the occurrence of serpentinites in the Hyblean basement [42] and neighboring offshore and onshore areas [46–48], including Mount Etna [49].

　　　The xenolith sample was taken from the tuff-breccia deposits cropping out in the middle section of the head wall of Valle Guffari. This is a bow-shaped valley, cut in the southeastern slope of Mount Lauro (986 m a.s.l.), in the central part of the Hyblean Plateau (Figure 1). Submarine basalts, Upper Pliocene in age (Figure 1e), overlay the aforementioned Miocenic tuff-breccia at about 850 m a.s.l., testifying the significant uplift of this area in the last 3–4 Ma [24].

3. Materials and Methods

　　　The vein-bearing peridotite xenolith displays an ovoid shape, 13.5 cm in length, 10 cm in width, with a thin, yellowish, alteration outer shell of clay minerals and Fe-hydroxides, as usual in peridotite xenoliths from Valle Guffari (e.g., Figure 1d). A rectangular block (about 6 cm long, 4 cm wide, 2 cm thick) was cut from the sample along with the vein of silicate glass (Figure 3a), and was used, hence, for thin-section preparation. Observations at a micrometer scale were performed on a TESCAN-VEGA\\LMU scanning electron microscope (SEM) at the Department of Biological, Geological and Environmental Sciences, Earth Sciences Section, University of Catania (Italy). Observations were made in backscattered electron (BSE) mode, under high vacuum conditions at 20 kV accelerating voltage and 0.2 nA beam current. Energy dispersive (EDS) micro-analyses were carried out using an EDAX Neptune XM4-60 system attached to the SEM, at an accelerating voltage 20 kV and beam current of 0.2 nA.

　　　Wavelength-dispersive analysis of major elements of the glass in the silicate vein and several olivine micrograins (Figures 2 and 3) and pyroxene crystallites (Figure 2), in the peridotite minerals as well, was performed using the JEOL JXA 8230 electron probe micro-analyzer (EPMA) at the Department of Biological, Ecological and Earth Sciences of the Università della Calabria (Cosenza, Italy). Calibrations were carried out using native metals and silicates as standard materials. Analyses were obtained under the following instrumental conditions: an accelerating voltage of 15 kV, a beam current of 10 nA, a beam spot of 10 μm, and an analysis time of 10 s. A detection limit of 0.01 wt.% was for all the detected elements. Results are reported in Tables 1 and 2.

　　　Major- and trace-element analyses were performed at the laboratory of SGS (Canada) on a fragment of the host peridotite xenolith. The fragment did not include the vein. The same chemical analyses were done in a portion of a coarse clast of the juvenile lava (nephelinite) from the tuffsite-breccia hosting the peridotite sample. The selected portions of samples were crushed and powdered with an agate mortar. Then, a weighted aliquot (~0.10 g) was digested by fusion with lithium metaborate in graphite crucibles and analyzed using ICP-AES and ICP-MS technical procedures. The concentrations of some trace elements (Cu, Ni, Pb, S, and Zn) were gathered by ICP-MS after the total digestion of the sample with four acids, beginning with hydrofluoric, followed by a mixture of nitric and perchloric acids. The accuracy of the method was determined by analyzing certified reference materials, while its precision was determined with replicate analyses (and found to be better than 10%). CO_2 was detected by coulometry, with 0.05% detection limit only in the peridotite whole-rock. Relevant analyses are concisely reported in Tables 1 and 2.

　　　Trace-element analyses in the vein glass were performed using the laser ablation ICP-MS technique at Istituto Nazionale di Geofisica e Vulcanologia (INGV), Palermo. A cut slice of the vein glass, about 2 cm in thickness, was polished before analysis. The analytical system consisted of an Agilent-7500 CX quadrupole mass spectrometer coupled with an ArF excimer laser ablation system (GeoLas Pro). During analysis, samples were maintained in a helium atmosphere, with a laser output energy of 15 J/cm^2, a repetition rate of 10 Hz, and a circular spot 32 μm in diameter. We used Ca as an internal standard and NIST 612 as an external standard. The NIST 612 analyses were carried out at the start, middle, and end of each analytical session. The precision was determined during each analysis session from the variance of ~15 NIST 612 measurements, which gave a relative standard deviation of $\leq 5\%$. The accuracy, calculated using the BCR-2 international standard, was $\leq 10\%$ for most of the elements.
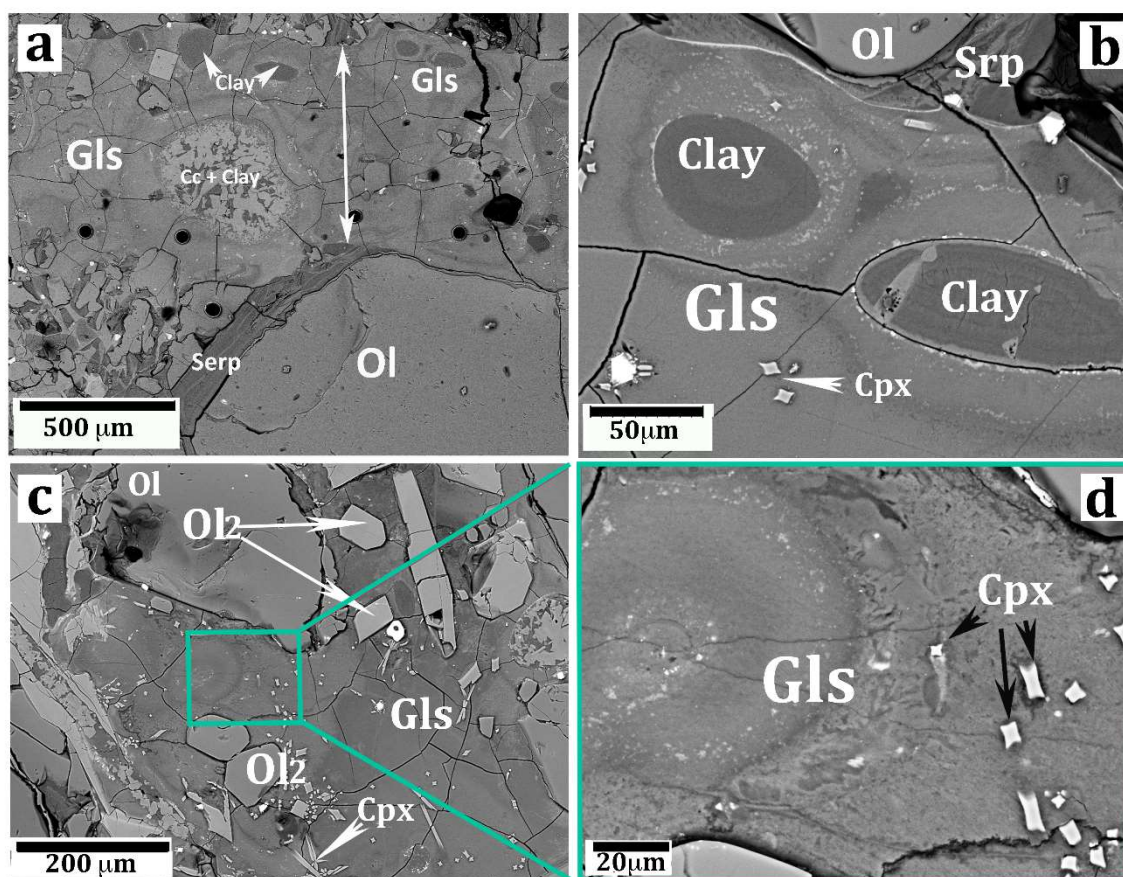
Figure 2. SEM images (backscatter mode) showing important aspects of the silicate glass vein. (**a**) A segment of the vein (the arrow highlights the vein width) showing a carbonate–clayey vesicle (Cc + Clay) and several smaller vesicles filled with saponite clay (same symbols as in Figure 3). The black circles are "craters" produced by the LA laser beam. (**b**) Two oval vesicles filled by clay (saponite). The glass near the edge of the vesicles is lower in Ti, Ca, and P with respect to the glass away from the vesicles (more information is given in the text). (**c**) A portion of the vein glass showing olivine micrograins (Ol2) and clinopyroxene chrystallites (Cpx) immersed in the glass. The relatively large olivine grain in the top-left picture is probably a disjointed fragment of the host peridotite olivine. A full explanation is given in the text. (**d**) High magnification of a portion of the previous picture (**c**) displaying the porous texture of the silicate glass.

Table 1. Major element distribution in minerals and sample whole-rock. (1–3) Representative microprobe (WDS) spot-analyses of quench clinopyroxene crystallites. (4) representative analysis of the olivine micrograins (average of 6 analyses). (5) Representative microprobe analyses of the clay mineral (saponite) filling the vesicles in the glass (average of 6 analyses). (6) Whole-rock analysis of the peridotite (harzburgite) xenolith hosting the vein glass. (7) Average composition of typical vein-filling serpentine minerals in the Hyblean peridotite xenoliths (from Reference [50]). (8) whole-rock analysis of a representative juvenile clast from the Valle Guffari diatreme tuff-breccia [32]. LOI = loss on ignition (minus CO_2 in 6); Bdl = below detection limits; nd = not detected. (*) = Total iron.

	1	2	3	4	5	6	7	8
wt%	Cpx	Cpx	Cpx	Ol	Sap	Harzb	Serp (Av)	Lava
SiO_2	47.43	45.37	49.33	39.63	37.18	41.70	41.14	38.42
TiO_2	2.66	3.14	2.21	0.38	0.10	0.02	0.02	1.93
Al_2O_3	6.81	8.02	4.74	bdl	13.46	1.92	1.52	12.47
FeO *	6.35	6.79	5.91	12.33	8.82	nd	8.63	nd

Table 1. *Cont*.

	1	2	3	4	5	6	7	8
Fe_2O_3 *	nd	nd	nd	nd	nd	8.60	nd	12.21
MnO	0.10	0.19	0.24	0.36	bdl	0.10	0.10	0.19
MgO	14.58	13.96	15.42	45.80	23.94	36.90	33.13	9.44
CaO	19.68	19.94	20.38	0.15	0.96	3.90	0.09	14.09
Na_2O	0.68	0.70	0.54	bdl	0.14	0.01	0.02	2.55
K_2O	bdl	bdl	bdl	bdl	0.08	bdl	0.02	1.15
P_2O_5	bdl	bdl	bdl	bdl	bdl	bdl	bdl	2.41
Cr_2O_3	0.62	0.32	0.57	0.17	bdl	0.03	nd	nd
NiO	bdl	bdl	bdl	0.31	bdl	0.02	nd	nd
CO_2	nd	nd	nd	nd	nd	1.70	nd	nd
LOI	nd	nd	nd	nd	nd	5.20	nd	4.92
Total	98.91	98.43	99.34	99.13	84.67	100.10		99.78
Mg#	81	78	82	87	83	89.50	87.30	60.70

Table 2. Representative microprobe (WDS) spot-analyses of the vein glass. Bdl = below detection limits. STDEV = standard deviation. (1) Average values of 15 spot-analyses in the brown-colored glass. (2–3) Minimum and maximum values. (4) Standard deviation values. (5) analysis (1) recalculated on anhydrous basis. (6) Average values of 16 spot-analyses in the green-colored glass. (7) Minimum, (8) maximum, and (9) standard deviation values. (10) analysis (6) recalculated on an anhydrous basis. A full explanation in the text.

	1	2	3	4	5	6	7	8	9	10
wt%	Average	Min	Max	STDEV	Av.Anhy	Average	Min	Max	STDEV	Av.Anhy
SiO_2	33.85	30.06	37.88	2.55	39.95	37.19	32.55	42.88	2.61	43.41
TiO_2	2.78	1.90	3.29	0.37	3.28	1.58	bdl	2.9	1.15	1.84
Al_2O_3	9.92	8.85	10.60	0.56	11.71	10.45	7.04	12.95	1.73	12.20
FeO*	9.63	8.26	11.73	1.13	11.37	12.22	7.91	14.23	2.20	14.26
MgO	20.35	17.29	22.91	1.64	24.02	22.81	19.65	26.49	1.75	26.63
CaO	5.64	4.00	6.50	0.82	6.66	1.14	0.84	1.27	0.13	1.33
Na2O	0.12	0.03	0.27	0.07	0.14	0.09	0.04	0.19	0.04	0.11
K_2O	0.11	bdl	0.21	0.06	0.13	0.13	0.06	0.23	0.06	0.15
P_2O_5	2.32	1.36	2.86	0.41	2.74	0.06	bdl	0.26	0.08	0.07
Total	84.71	81.29	88.15	2.76	100	85.67	81.75	87.23	1.57	100
* tot.	n=16					n=15				

4. Optical and SEM Petrography

Although about 30% by volume of the sample consisted of serpentine minerals, a primary harzburgite composition (serpentine + olivine = 60 vol%, Ca-poor pyroxene = 33%, clinopyroxene = 3%, spinel = 4%) was still clear. Microprobe spot analyses in a polished, carbon coated, thin section of the sample indicated that olivine was a forsterite (Fo_{91}); orthopyroxene was an enstatite (En_{90}; Al_2O_3 = 3.8 wt%); clinopyroxene was Cr-diopside ($En_{56}Wo_{38}$; Al_2O_3 = 4.5 wt% and Cr_2O_3 = 1.3 wt%); and the brownish spinel was a picotite, with Cr# = 0.30 and Mg# = 0.76, where Cr# was Cr/(Cr + Al) and Mg# = Mg/(Mg + Fe). The grain size of this rock was highly variable because of the ubiquitous occurrence of neoblastic subgrains, with different grain-sizes, after primary, coarse (up to 3 mm) olivine grains. Serpentine formed a complex network of veins that that pass through both the porphyroclast and subgrain olivine grains. Serpentine veins in some peridotite xenoliths from Valle Guffari, close to and similar to the sample, were studied by [50]. The veins generally consisted of two polytypes, chrysotile $2M_{c1}$ and lizardite 1*T*. Serpentine veins in the sample were coaxially intruded by a late vein of microcrystalline, Sr-bearing, low-Mg, Ca carbonate (likeky aragonite [51]). Ni-rich sulfide (e.g., millerite-NiS: Reference [50]) and magnetite micrograins, as by-products of the serpentinization reactions [35,49], were evenly distributed along the serpentine veins. A further set of late-stage

carbonate veins, either parallel or discordant with respect to the serpentinite veins, also occurred in the sample (Figure 3d; Reference [51]).
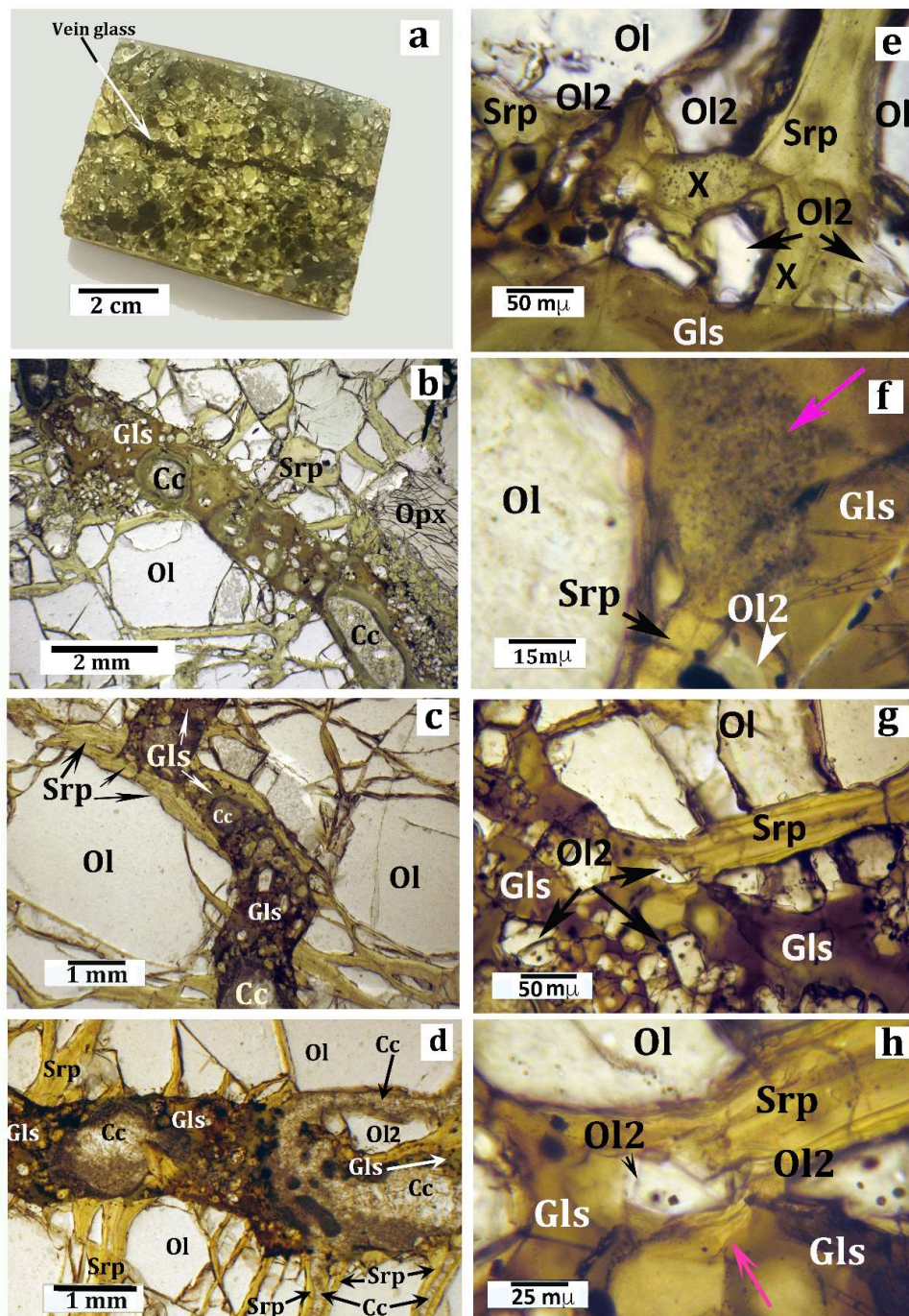
Figure 3. Macroscopic (**a**) and microscopic (**b**–**h**) pictures of the sample, with discussion as reported in the text. All microphotographs were taken under the optical microscope in plane-polarized light. (**a**) A small rectangular block cut in the host peridotite xenolith, used for thin-section preparation. The arrow indicates the silicate glass vein. (**b**) Detail of a thin section showing a typical segment of the vein. Full description is given in the text. (**c**) Microphotograph (plane-polarized light) highlighting that a short segment of the vein is intruded in a previous serpentine vein. Legend for (**b**) and (**c**): Gls = silicate glass; Ol = olivine; Srp = serpentine (± talc, ± chlorite); and Cc = carbonates (aragonite in most cases

[51]). (**d**) Microphotograph showing veins of secondary carbonate minerals postdating the serpentine veins and the silicate glass vein. The connection between a carbonate vein and one of the carbonate vesicles in the silicate glass is highlighted. (**e**) Microphotograph showing the contact (reaction) zone between a narrow serpentine vein (Srp), perpendicular to the glassy vein, and the silicate glass (Gls). Ol2 = olivine microcrystals representing products of the serpentine dehydroxylation; X = amorphous and/or cryptocrystalline material produced by the serpentine breakdown (more explanation is given in the text). (**f**) Contact zone between a serpentine vein (Srp) and the vein glass (Gls). Here the reaction products form an opaque mineral-rich "plume" starting from the vein. The pink arrow indicates the opacitic "plume". Other symbols as in previous pictures. More explanation is given in the text. (**g**) Microphotograph showing a contact zone between a serpentine vein (Srp) perpendicular to the glassy vein and the silicate glass. The area is crowded by tiny reaction olivine micrograins (Ol2). (**h**) Close view of the central area of the previous picture (**g**) highlighting the relationships between the serpentine (Srp) reactant and an olivine micrograin (Ol2) as one of the reaction products. The pink arrow indicates a relict shred of the serpentine reactant.

A roughly straight vein (Figure 3a) of dark-gray silicate glass, 1–1.5 mm in thickness, crossed the sample according to the minor axis. At a microscopic scale (Figure 3b,c), the vein walls appeared fairly irregular because the olivine subgrains at the vein wall rotated at different angles.

Observations in thin section under the optical microscope made it clear that the glass vein crossed the serpentine veins occurring along its track. Interestingly, a short segment of the glass vein coaxially intruded a segment of a serpentine vein (Figure 3c). Where an orthopyroxene grain occurred at the vein walls, the former appeared widely replaced by a selvage of reaction olivine micrograins, 1–10 μm in size, (e.g., right-bottom of Figure 3b). Many olivine (Fo_{87}) micrograins and much smaller skeletal crystallites of clinopyroxene (Mg# = 75–81: Table 1; Figure 2b–d) were immersed in the glass. The olivine micrograins generally displayed rounded, tiny brownish inclusions considerably more Fe-rich than those from the harzburgite of unidentified material and magnetite (Figure 3e–h). In addition, many of vesicles filled with carbonate and/or clay minerals crowded the vein glass along its entire length (Figure 3b,c; Figure 2a,b). Some carbonate vesicles displayed an elongated shape according to the vein trend (Figure 3b) with their short axes being often as large as the vein width. One of the numerous carbonate veins irregularly crossed the sample, flowing into a carbonate vesicle present in the silicate glass vein (Figure 3d).

The glass was semitransparent, with an irregular color zoning from brownish (more common) to green, the latter color generally occurring all around the carbonate/clay vesicles. Observations in cross-polarizer mode testified the perfectly isotropic character of both brown and green glass. SEM images evidenced an irregular set of fractures in the glass and, more importantly, its highly porous texture at the sub-micron scale (Figure 2d).

5. Analytical Results

Whole-xenolith major element distribution, including CO_2, (methods in the previous section) is reported in Table 1 (Analysis 6). Allocating the entire CO_2 content (1.7 wt%: Table 2, Analysis 6) of the whole-rock to Ca carbonate, a normative (CIPW) 4.09 wt% (4.92 vol%) of $CaCO_3$ can be calculated, which agreed with the estimated modal occurrence of carbonate veins in the sample. Accordingly, the amount of remaining CaO (2.25 wt%) available for silicate minerals was consistent with the modal abundance of clinopyroxene.

Several microprobe spot analyses were performed on a segment of the vein, prepared as a thin section of standard size according to its long side. Results are summarized in Table 2. In general, the glass analyses displayed very low totals (81–88 wt%). This fact may indicate the occurrence of an unidentified, probably volatile, component in the glass, or it may depend on missing beam counts because of the aforementioned porous texture of the glass (Figure 2d). Most likely, both factors (volatiles and analytical artifacts) concurred to give low totals. Considering the glass far away from the vesicles (i.e., the brown colored type), MgO varied between 17.3 to 22.9 wt%. The average value of

15 spots was 20.35 wt% (Analysis 1 in Table 2), increasing up to 24.02 wt% when recalculated on an anhydrous basis (Analysis 5 in Table 2).

The green glass displayed slightly higher MgO values than the brown glass (Table 2). The differently colored glasses also displayed slightly different Al_2O_3 contents (9.92 wt% on average in the brown glass and 10.45 wt% in the green glass with 11.7 and 2.2 wt%, respectively, on an anhydrous basis; see Table 1, Analyses 6–10). Na_2O and K_2O were often below 0.1 wt% (Table 2) in both brown and green glasses. On the other hand, the brown and green glasses significantly differed in TiO_2, CaO, and P_2O_5 content, which were higher in the former than latter (Table 2). It must be remarked that the content in TiO_2 was >1 wt% in both brown and green glass, with rare exceptions. Conversely, FeO (here reported as total iron) in the brown glass (9.6 wt% on average) was lower than green glass (12.2 wt%). Representative trace element analyses of the vein glass, as obtained by ICPMS-Laser-Ablation spots along a 1 cm-long section of the vein, are reported in Table 3. Although the microscope of the ICPMS-LA equipment did not allow to distinguish between brown and green glasses, we took analyses both at the rim of carbonate/clay vesicles, where the green glass occurred, and away from the vesicles, where the brown type occurred. No discrimination between the two differently colored glasses was possible on the basis of trace element distribution. As indicated by the standard deviation values, the composition of the glass vein was quite heterogeneous at the micrometer scale with respect to several trace elements (in particular Cr, Ni, Sr, and LREE).

Table 3. Trace element analyses of the vein glass, the harzburgite xenolith, the host lava and serpentine veins. (1) Average of 15 spot-analyses by ICPMS-LA in different areas of the vein glass. (2) Minimum, (3) maximum, and (4) standard deviation values. (5) Trace element analyses of the harzburgite (Harzbur.) xenolith hosting the glassy vein. (6) Trace element amounts of a representative juvenile clast from the Valle Guffari diatreme tuff-breccia [32] (host lava). (7) Average of spot analyses in serpentine (Serp.) veins in representative Hyblean peridotite xenoliths (after Reference [50]). Bdl = below detection limits. Nd = not analyzed. (*) = Total iron. A full explanation is given in text.

	1	2	3	4	5	6	7
	Glass				Harzbur.	Host Lava	Serpent.
ppm	AVER.	MIN	MAX	STDV			
Cr	153.73	48.79	413.94	108.13	2867	380	306
Co	45.20	28.45	63.08	11.76	113.20	51	nd
Ni	262.18	110.77	478.66	132.67	2046	269	nd
Rb	2.64	1.09	7.23	2.07	0.66	23	3.41
Sr	602.17	453.76	933.08	159.70	195.10	1960	8.02
Y	34.18	27.90	49.62	7.19	0.61	26	0.17
Zr	275.61	221.69	383.72	59.53	2.03	135	0.52
Nb	116.50	82.52	158.61	31.44	0.71	141	0.16
Ba	82.01	39.68	228.33	64.54	1.50	1290	nd
La	122.63	83.63	163.47	28.48	1.31	140	0.16
Ce	225.97	164.67	324.28	50.37	2.12	281	0.36
Pr	23.99	18.18	33.79	5.10	0.26	33	nd
Nd	88.12	70.28	125.02	17.93	0.80	119	0.20
Sm	14.46	11.96	19.97	2.63	0.11	20	0.03
Eu	4.22	3.37	6.00	0.78	0.02	5.5	0.04
Gd	15.75	12.87	22.33	3.15	0.12	15	0.03
Tb	1.55	1.33	2.17	0.29	0.01	1.49	nd
Dy	8.07	6.39	11.75	1.78	0.02	8.00	0.02
Ho	1.34	1.07	2.01	0.33	0.01	1.30	nd
Er	3.34	2.72	4.54	0.63	0.13	3.30	0.02
Tm	0.43	0.33	0.59	0.10	0.01	0.39	nd
Yb	2.60	2.02	3.88	0.61	0.1	3.00	0.03
Lu	0.36	0.28	0.50	0.08	0.01	0.40	nd
Hf	5.42	4.18	7.12	1.07	0.09	4.55	nd
Ta	5.24	3.81	7.20	1.36	0.03	5.30	nd
Pb	3.84	1.58	8.99	2.43	0.31	4.21	nd
Th	11.45	8.57	16.86	2.65	0.11	11.1	nd
U	3.55	2.43	5.48	0.93	0.05	2.91	nd

6. Discussion

Literature reported on patches of silicate glass, a few millimeters in size, in the Hyblean ultramafic xenoliths have been ascribed to local partial melting of eutectoid mineral assemblages [52,53] as a result of transient heating of the xenoliths, as entrained in the eruptive system. In addition, veins of silicate glass, with roughly basanite composition, were also observed in some peridotite xenoliths that have been related to mantle metasomatism [54].

Microscopic observations of the sample studied clearly indicates that the glass vein postdates the serpentinite veins (Figure 3b–d). This fact excludes the possibility that the silicate melt (now glass) infiltrated into the sample at mantle depths, since serpentinization is a low-temperature (< 500 °C) process [55], which requires plenty of reactant water, seawater in most cases [56,57], and an adequate fracture system through which seawater can penetrate. Serpentinization typically occurs (although not only) in the oceanic lithosphere, particularly along slow-spreading ridges [58,59]. As previously mentioned, geophysical data suggest the occurrence of serpentinites and highly serpentinized peridotites in the unexposed basement of the Hyblean and neighboring areas [42]. It is therefore reasonable to assume that the same pre-Triassic basement has been widely serpentinized also in the late Miocene, when the xenolith-bearing diatreme eruptions occurred. In this respect, [16] put forward, in a preliminary way, the hypothesis that the Hyblean diatremic eruptions resulted from the explosive interaction between serpentinite bodies and upwelling mafic magma at shallow/middle crustal depths. Manuella et al. [17] later developed and substantiated such a hypothesis, particularly addressing the thermodynamic aspects of the process.

The carbonate veins in the sample clearly postdates both the serpentine and the glass vein. Moreover, the connection between the carbonate veins and carbonate vesicles in the glass is evident (Figure 3d). Thus, a primary origin of the carbonate vesicles (e.g., as immiscible carbonatite bubbles) can be reasonably ruled out. Such a conclusion is strengthened by the occurrence of 0.5–1.5 wt% strontium in both vein and vesicles carbonate, as revealed by microprobe analyses. This suggests an aragonite polytype, which is the typical carbonate mineralization in abyssal serpentinites, albeit outside its stability field [51].

Major element distributions may be used as proxies for a petrological classification of the vein glass, following the IUGS recommendations for high-Mg and picritic volcanic rocks [60,61]. MgO (> 18 wt%) and $Na_2O + K_2O$ (< 1 wt%) either correspond to a meimechite or komatiite composition, whereas TiO_2 (> 1 wt%) fits in the latter. In this respect it is worth to mention that some authors do not recommend the general use of the term "meimechite", which, according to [62], should be applied only to "highly magnesian high-Ti picrites with a great number of coarse-porphyritic olivine grains and an abnormally high content of incompatible and rare-earth elements which occur in the Maimecha River basin". On the other hand, Al_2O_3 (11.7 wt%) and P_2O_5 (2.7 wt%) contents in the brown glass are out of the range for meimechite (and komatiite) compositions, conforming to an alkaline picrite instead [63].

The occurrence of color and compositional zoning in the vein glass is still an open problem. The fact that the green glass occurred only near the carbonate and clay vugs may suggest that some fluid-induced element diffusion between the glass and the nearby saponite vug occurred. Henceforth, we consider only the high-Ti, high-P (brown colored) glass for discussion, and we regarded the green glass as an alteration product.

Despite the very low content in alkalis (Table 2), trace-element abundance (Table 3) and some distinctive element ratios (e.g., Nb/Yb = 3.4; Zr/TiO_2 = 99 [63]; Nb/Yb = 45; Figure 4a), Ce_N/Yb_N = 23, indicates the alkaline affinity of the intruding high-Mg melt, which displays an OIB signature, e.g., ΔNb [1.74 + log(Nb/Y) − 1.92 log(Zr/Y)] = 0.5 [64]; Th/Yb = 4.4; Ta/Yb = 2 [66] (Figure 4b). It is worth to mention that geochemical and isotopic research on Hyblean alkaline volcanic rocks, such as alkalibasalts and nephelinites, indicated an OIB (and HIMU) signature in their mantle source [25,26,29–31].
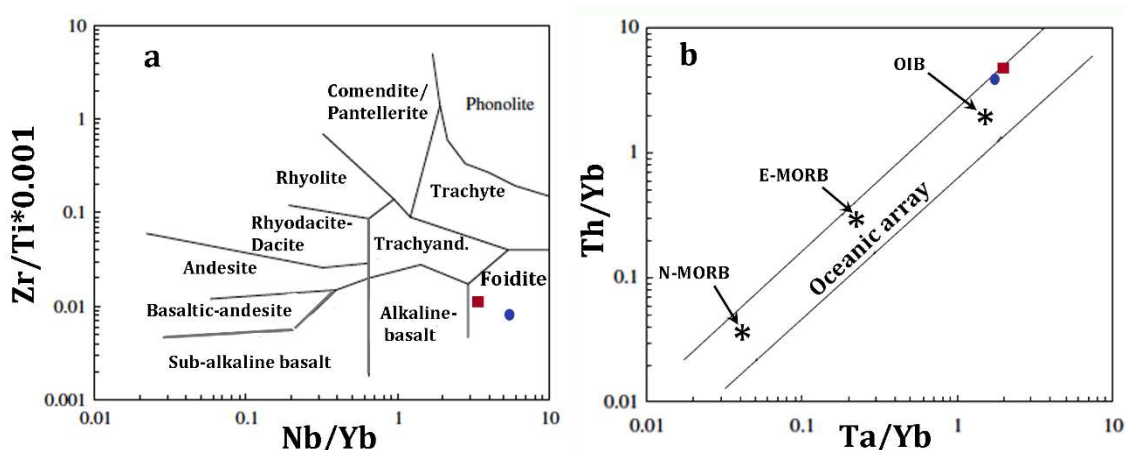
Figure 4. Petrologic discrimination diagrams for the vein glass (average composition) and the juvenile lava in the tuff-breccia deposits in Valle Guffari. Squares and circles indicate the vein glass and the juvenile lava, respectively. (**a**) Nb/Y–Zr/Ti classification according to [64]. (**b**) Ta/Yb vs Th/Yb diagram, simplified after [65], where igneous rocks from intra-oceanic plates are included in the area between the parallel lines.

In general, abundances in compatible trace elements in the glass (e.g., Cr = 154 ppm; Ni = 262 ppm, on average; Table 3) are relatively low, and abundances in incompatible elements are relatively high, with respect to a high Mg content (Table 2; Figure 5). This geochemical paradox forms the main difference between the considered glass and the worldwide high-Mg volcanic rocks with alkaline affinity, which display compatible element abundances consistent with an ultramafic composition. For example, Reference [67] concluded that the meimechite primary magma had MgO from 25 to 27 wt%, NiO ~1000 ppm, and Cr_2O_3 ~2000 ppm.

The N-MORB normalized multi-element variations (Figure 5) shows that almost all spot analyses in the silicate glass display sub-parallel patterns, indicating the coherent variation in elements with similar geochemical behaviors between the set of analyses, despite considerable differences in absolute abundances of some elements. Interestingly, the same "compatibility" diagram shows that trace element distribution in the vein glass closely matches the nephelinite juvenile clasts occurring in the tuff-breccia (Table 3; Figure 5).

On the above premises, we put forward the hypothesis that a mantle-derived nephelinite melt, with MgO = 7–10 wt%, encountered buried serpentinites bearing relics of serpentinized peridotite at an unknown depth en-route to the surface through a crustal tectonic discontinuity. As previously mentioned, there is geophysical inference on such buried serpentinites in the Hyblean area [42], and is compatible with the Mesozoic oceanic core complex hypothesis [33–35].

The thermodynamic aspects of the interaction between mafic magmas and serpentinites at crustal depths, chiefly related to the formation of diatreme systems, were discussed by [17]. Here we tentatively address the same issue from the geochemical and petrologic perspectives, focusing on the non–explosive interaction processes, even though no quantitative approach is allowed, because of the obvious disequilibrium conditions of the invoked processes. We recall some general concepts on serpentinization, experimental results, and theoretical models on serpentine dehydroxylation processes, which are pertinent to the discussion.
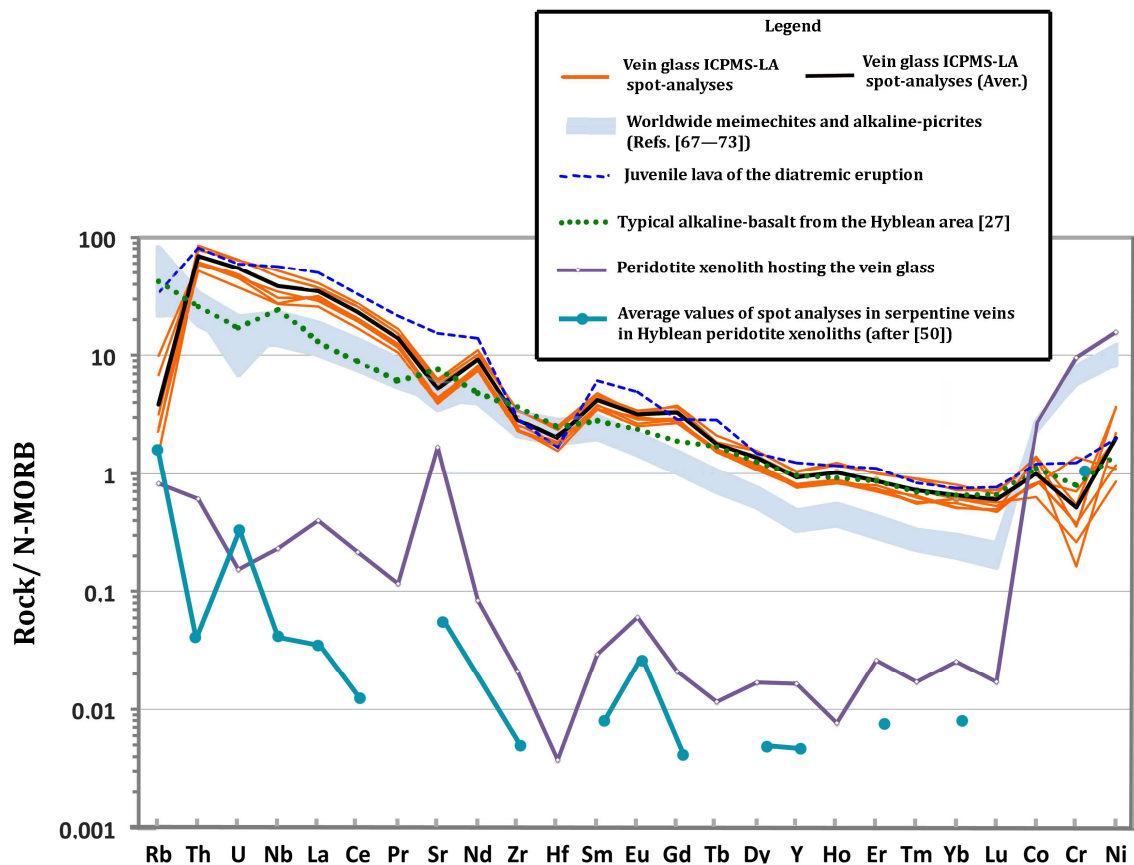
Figure 5. Compatibility diagram (sample vs. normal-MORB) of the vein glass ICPMS-LA spot-analyses, the juvenile lava of the diatremic eruption, a typical alkaline-basalt from the Hyblean area [27], the peridotite xenolith hosting the vein glass and the average values of spot analyses in serpentine veins in Hyblean peridotite xenoliths (after [50]) as indicated in the Legend. The shadowed area represents published analyses of worldwide meimechites and alkaline-picrites (References [67–73]). N-MORB normalizing values after [74].

Modern and ancient abyssal-type serpentinites can be considered as low-temperature geological bodies (e.g., $300 \leq T \leq 500$ °C) [75,76]. Hence, a temperature increase is one of the major effects produced by the interaction with an upwelling mafic magma, with a temperature typically in the range 1100–1250 °C [77,78]. Because a magmatic intrusion cools by conduction, the heat transfer rate increases with the increased surface area. The serpentinite heating is, therefore, more effective if the magma can spread through a wide fracture network. This is a common feature in ultramafic bodies undergoing serpentinization, as the process develops via a crack-and-seal mechanism [79]. Experimental studies demonstrate that the interactions occurring at confining pressures above the critical point of water (22 MPa) is generally non-explosive, since no liquid–vapor phase boundary exists in supercritical fluids, including water. Moreover, the thermal energy released by the interaction between magma and geological bodies that contain water is partitioned into different forms, including non-explosive chemical processes such as solution and precipitation as well as mass diffusion [80].

The dehydration of serpentine polytypes (Lizardite, Chrysotyle, and Antigorite) can develop [81] in the thermal range of 450–800 °C. The loss of structural water depends on the interlayer bond strength of serpentine polytypes, ranging from 12.3 wt% in antigorite to 16.3 wt% in chrysotile [81]. Thermodynamic calculations [56,82] at a pressure range of 0.1–0.2 GPa show that serpentine dehydroxylation develops at a temperature ≥ 400 °C, producing forsterite, talc, and water. At higher temperatures (T > 600 °C), forsterite reacts with talc, generating anthophillite and water, whereas forsterite and anthophillite produce enstantite and water at about 670 °C [82].

In the vein glass there are lots of olivine micrograins (Figure 3f–h), too large to be quench phases, which most likely are reaction products of the serpentine breakdown. According to Reference [83], olivine produced by serpentine dehydroxilation may host inclusions of magnetite, serpentine, and hydrous fluids, as it occurs in most of the aforementioned olivine micrograins. Magnetite as a reaction product may indicate that the serpentine reactant was bearing some iron, as highlighted by Reference [50]. Alternatively, iron that formed magnetite was mostly derived from the reactant silicate melt. The formation of either talc or enstatite as reaction products has been likely inhibited by the silica-undersaturated composition of the reactant nephelinitic melt. Nevertheless, the occurrence of reaction products other than olivine, fine-grained enough to elude optical microscope observation, may be inferred from the turbid patches in the silicate glass in close contact with serpentine (Figure 3e).

On the other hand, experimental results and thermodynamic calculations [56,84] evidenced that the serpentine breakdown is a heterogeneous process, because of the occurrence of significant reaction energy barriers. The dehydroxylation of serpentine polytypes at ambient pressure occurs stepwise in a temperature interval. Hence, one or more metastable phases, either crystalline or amorphous, develop along the reaction path, especially at relatively low temperature conditions (500–600 °C). For example, chrysotile and lizardite, both representing the typical serpentine polymorphs in oceanic abyssal settings, at temperature of about 380 °C metastably decomposes to form the antigorite polytype and forsterite, hence, it releases water [56].

Moreover, Gualtieri et al. [84], during the dehydroxylation of antigorite by progressive heating at ambient pressure, noticed the formation of metastable talc nuclei and an amorphous magnesium oxide:

$$Mg_3Si_2O_5(OH)_4 \rightarrow 1/2\ Mg_3Si_4O_{10}(OH)_2 + 3/2\ MgO + 3/2\ H_2O. \tag{1}$$
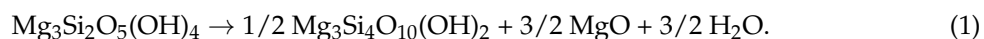
In the case study, the occurrence of (possibly metastable) solid particles, even at a nanometric scale, is likely indicated by the turbid aspect of some reaction "plumes" at the contact between serpentine veins and the silicate glass, as evidenced under an optical microscope (e.g., the zone indicated by the colored arrow in Figure 3f).

At higher temperature values (700–800 °C), forsterite and enstatite crystals, a few nanometers in size, begin to form [84]. On the other hand, hydrated monocationic complexes, such as $[Mg^{2+}(H_2O)_n]$ (n = 5–7 [85,86]), can develop in hydrothermal systems. In particular, there is evidence for the formation, at T > 300 °C, of a complex with the configuration $[Mg(H_2O)_n\ (H_2O)]^{2+}$, where the additional (H_2O) denotes the presence of a water molecule that occupies an outer solvation shell, which is also hydrogen bonded to one or more molecules in the primary shell [86].

The mafic magma involved in the serpentine breakdown process loses energy and cools. On the other hand, it is a general principle of igneous petrology that water lowers solidus temperatures of different igneous systems [87]. A typical abyssal serpentinite contains up to 13 wt% of water [81] in the form of structural OH groups. The hydrous fluid released by serpentine minerals may, therefore, let the liquid fraction of the intruding magma persist through the entire interaction processes. The lowering of the magma viscosity resulting from the flushing of volatiles is even greater if the system contains in itself a considerable amount of magmatic volatiles, including H_2O.

Considering serpentinites located at a depth between 5 and 15 km below the seafloor, i.e., at a pressure P >> 22 MPa, the hydrous fluid released by the breakdown reactions (T > 374 °C; P ≥ 22 MPa) attains a supercritical state, which has, therefore, a chemically aggressive behavior [79]. Most likely such fluid is able to extract large ion lithophile elements from the surrounding rocks/melt and, hence, incorporates the Mg-rich, metastable products of serpentine breakdown (e.g., reaction 1) in the form of solutes and/or complexes and/or finely dispersed nanoparticles. Moreover, the aqueous fluid likely flushes [88] into the interacting nephelinite magma. As a consequence, non-explosive mixing/mingling processes [89] can occur, giving eventual rise to the hybrid, high-Mg, hydrous silicate magma mentioned in the previous section. In other words, the shifting of the nephelinite solidus (and liquidus) curves towards lower temperatures, resulting from the addition of the aqueous fluid to the system, could compensate for magma quenching by conductive cooling. Thus, the

low-viscosity, high-Mg silicate melt could likely infiltrate into the fracture systems of the surviving, less-serpentinized relicts of the original ultramafic body. In the case study, a fragment of the melt-veined rock was entrained as xenoliths in the diatreme system. The rapid degassing and quenching of the melt at shallower depths formed the vesicles (Figure 3b) and the porous texture (Figure 2d) of the vein glass.

Substantiating the aforementioned hypothesis by thermodynamic numerical modeling and/or precise geochemical mass-balance calculations is hampered by the intrinsic heterogeneity of the invoked process and by-late stage chemical transformations because of the circulation of low-T, aqueous, and carbonate fluids. This fact is testified by the secondary clay and carbonate minerals filling the vein vesicles (Figure 3d, Figure 2).

A comparison of the major element distributions between the glass and the serpentine and nephelinite end-members is shown in Figure 6. Here, the average values of each end-member and the maximum and minimum values in the glass, as reported in Table 2, are indicated with different symbols (see the Figure 6 caption). Major elements in the glass are compatible with mixtures in different proportions of the serpentinite and nephelinite end-members (Figure 6). For example, MgO in the glass is compatible with a mixture of 45.4 wt% nephelinite and 54.6 wt% serpentine, and FeO is compatible with a mixture of 53 wt% serpentine and 47 wt% nephelinite. CaO in the glass may be caused by the mixture of 60 wt% serpentine and 40 wt% nephelinite; a mixture of 80 wt% nephelinite and 20 wt% serpentinite can be accounted for the Al_2O_3 in the glass. The silica content in the glass is lower than both end-members, and is not consistent with the mixture. This fact may be explained by the occurrence of abundant brucite in the original serpentinite system, though further investigation is necessary to adequately address this problem.

In general, the fact that different chemical elements in the same melt (now glass) result from different proportions of the two geochemical end-members (Mg-rich products of the serpentine breakdown and nepheinite magma) may depend on the different diffusive velocities of the involved chemical elements [90–92]. This fact has been numerically addressed by [83,84] from the "concentration variance" [91] and "Shannon entropy" [92] perspectives, respectively, even though the magma types considered by the aforementioned authors were rhyolitic and basaltic. In the case of magma mixing, both parameters are different for different chemical elements, each having different mobilities in the mixing system. Such a mobility difference is enhanced when the mixing process develops rapidly (hence, ends abruptly), as in the case of quenching of silicate melts [91].

The extremely low content in alkalis of the melt may be apparent, since the huge increase in Mg and water, as above described, has reduced the quantity of the previous components, including alkalis. On the other hand, there is a relatively high abundance of other minor elements, such as P and Ti, in the same glass (Table 2). Excluding analytical artifacts, part of the alkalis may have been partitioned in the gaseous phase during the serpentine–magma interaction. The hybrid, Mg-rich, melt largely retained the trace element distribution of the original nephelinite, as shown in the multielement variation diagram in Figure 5. In the same spider-diagram a typical Hyblean alkalibasalt is also reported, indicating that such a rock composition cannot be used as the end-member, always displaying lower amounts in incompatible trace elements than the vein glass (Figure 5).

In general, we suggest that the interaction between mantle-derived primitive magmas, including any types of basalts, basanites, nephelinites, and subjacent serpentinites, is a plausible way to explain the volcanological paradox of large explosive eruptions produced by high-Mg magmas, which normally give rise to quiet effusive eruption [3]. With respect to the case of the ancient picritc explosion that occurred in the eastern flanks of Mount Etna, as reported by [9], it is plausible to hypothesize that serpentine, possibly in form of diapirs, occurs beneath this volcano, since serpentinites occur in the Hyblean lithospheric domain [42,46], which is generally thought to be the same as Mount Etna [24,39]. Accordingly, Correale et al. [93] highlighted the geochemical similarity of the mantle sources feeding the volcanic activity of Mount Etna and the Hyblean Plateau. The same authors also presented a geochemical model suggesting that different degrees of partial melting of a Hyblean-like mantle, in

the pressure range 1–2 GPa, with the addition of about 0.03–0.1 wt% H_2O, can give rise to different mafic melts that includes the entire geochemical spectrum of the Etnean magmas.
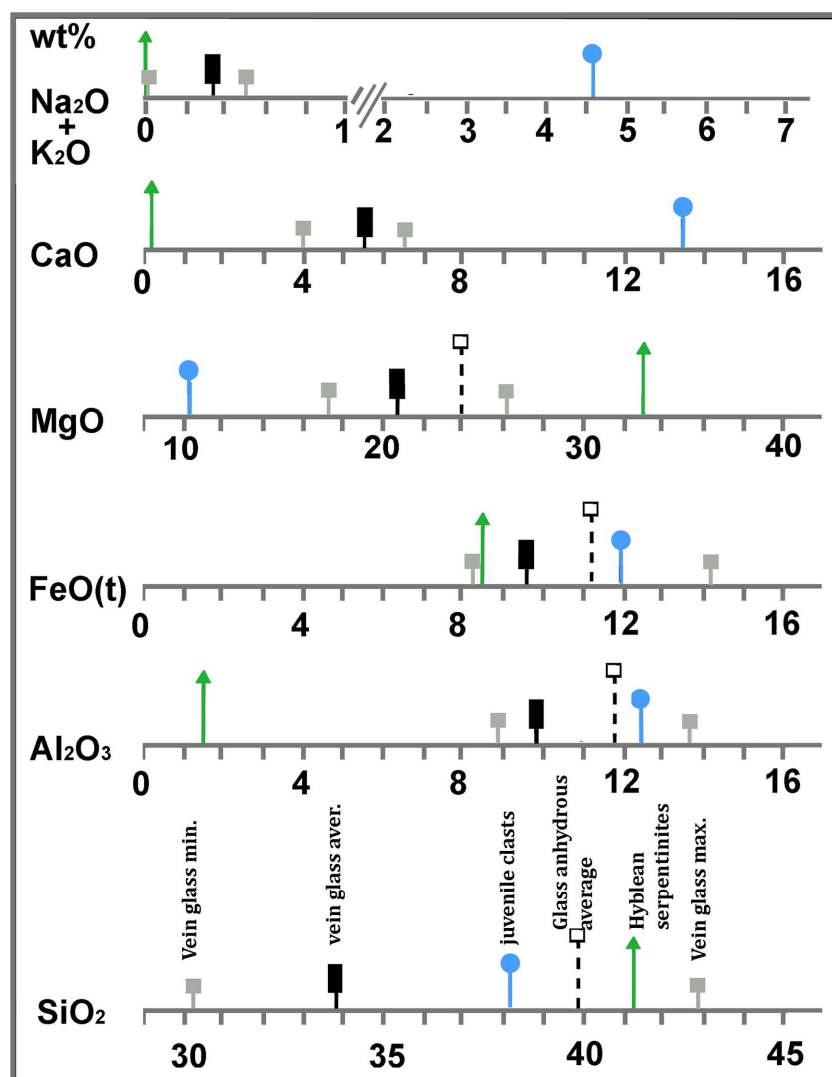
Figure 6. Synoptic table showing relationships between major element distributions (average) in the Hyblean serpentinites (triangle), the vein glass (rectangle), and the nephelinite volcanic rock that forms the juvenile clasts of the xenolith-bearing tuffsite breccia (circles). Full squares indicate minimum and maximum values. Open squares indicate average values recalculated on an anhydrous basis. Serpentine mineral analyses were reported after [50]. A full discussion is given in the text.

High-Mg magmas are generally thought to have origins through high percentages of mantle melting [94]. This fact would imply a very high temperature. The dry, one-atmosphere *liquidus* temperature of melts with MgO contents between 28% and 30%, calculated from experimental data [63], is reported between 1560 and about 1600 °C. A phase equilibrium experimental study reported by [22] indicated that a primary meimechite magma with 1 wt% water originated at ~5.5 GPa and 1700 °C. Previous experimental data [19,63] suggested that the stability of orthopyroxene and garnet, relative to olivine, increases with pressure (depth). Hence, more magnesian magma forms as pressure increases above about 8 GPa (about 250 km in depth) near solidus melts that contain more than 30 wt% MgO. In these P-T conditions, komatiite magma forms through 30–50% melting, leaving a residue of olivine and majorite garnet [23,94]. On the other hand, the formation of a high magnesian magma rich in incompatible elements (e.g., meimechite) would require a very low degree (≤ 3%) of partial

melting [22]. Moreover, at pressures greater than about 8 GPa the density of an ultramafic (either komatiite or meimechite) liquid exceeds that of olivine, which is however slightly lower than that of the olivine plus garnet assemblage [95]. These facts pose some concerns on the mobility of small quantities of such incompatible element-rich, high-Mg liquids through the source rock, to coalesce in relatively large pools, and eventually to be subjected to a $\geq$ 250 km-long ascent through the lithosphere, where they may achieve neutral buoyancy.

The scarcity of picrites in most flood basalt successions has been ascribed to density trapping of the primary Mg-rich melts in sill-like complexes at the crust–mantle boundary [96]. In addition, such high-Mg, silica-undersaturated liquids are highly reactive [94,97] and, hence, the possibility that they will reach shallow crustal levels with no significant chemical modifications may be quite low. Adding volatiles to the system dramatically increases the mobility and buoyancy of such magmas, even though their reactivity would be enhanced, especially in the case of a high percentage of CO_2 in the volatiles [98]. Aqueous fluids, nevertheless, may not be abundant at mantle depths, as evidenced by the very rare occurrence of hydrous minerals in mantle xenoliths worldwide [99]. In the Hyblean case, a thirty-year detailed study of several tens of xenolith samples evidenced only two crystal grains of phlogopite from one peridotite xenolith [100] and a few pargasite grains in just two pyroxenite samples [53]. Of course, we do not disprove the generally acknowledged hypothesis that ancient subducted oceanic slabs have introduced fluids in the mantle, even though here we express the opinion that too many exceptional conditions, as above mentioned, would occur to let meimechite and alkali-picrite magmas form at mantle depths and, hence, give rise to volcanic eruptions.

On the other hand, some authors suggested that ultra-magnesian magmas are not primary mantle melts, since olivine was subsequently added to a primitive, less magnesian magma, to create a meimechite, komatiite, or kimberlite bulk composition [101,102]. Of course, the aforementioned hypothesis cannot explain the occurrence of poorly porphyritic, even aphanitic, high-Mg melts [63] that formed the studied vein glass. Our data instead indicate that some meimechite and alkali-picrite melts, in different geological contexts, may be produced by the interaction of mafic (e.g., basalt) primary magmas with serpentinites at different crustal levels. Of course, we are aware that our point of view needs to be strengthened by further investigations, both in the field and in the laboratory.

7. Conclusions

The data reported and discussed in this paper lead to the following conclusions:

(1) The widely acknowledged idea that "the very small" can be helpful to understand the "very large" is here plainly verified: the thin vein of silicate glass in the fist-size peridotite xenolith gives important information to clarify the volcanological paradox of large explosive eruptions produced by high-Mg magmas, which generally yield quiet effusive eruptions.

(2) The interaction between mafic magmas, undersaturated in volatiles, and subjacent serpentinites is a plausible way to explain the formation of a hybrid silicate melt very rich in Mg and in volatiles, chiefly H_2O. Since serpentinite is very much depleted in incompatible elements, compared to the igneous end member, the latter can impart its geochemical signature to the newly formed, hybrid melt.

(3) Some ultramafic volcanic rocks, including some komatiite, meimechite, and (alkali-)picrite types, in diverse geological contexts, may derive from hybrid melts produced by the interaction of primitive mafic magmas (e.g., basalts) with serpentinites at crustal depths (Figure 7). Although serpentinites chiefly originate in abyssal oceanic settings [56–59], buried serpentinite bodies very likely occur at shallow/middle crustal depths worldwide, even in Mediterranean-type marine basins [103] and in cratonic areas.

(4) The Aforementioned suggestions can be relevant to explain some ancient and recent explosive eruptions of Mount Etna, related to relatively Mg-rich, even picritic [9] magmas, although some background geological problems are still debated among researchers (e.g., whether serpentinite geological bodies occur in the Etnean basement, or not).
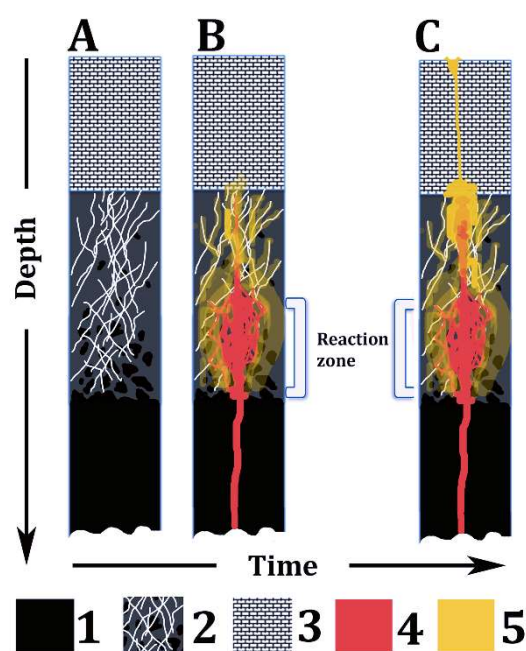
Figure 7. Summary sketch of the model proposed in this paper. A, B, and C represent the same lithospheric section over time. Legend: (1) Ultramafic rocks of the upper mantle; (2) Fractured serpentinite, bearing relicts of partially serpentinized ultramafic rocks; (3) Shallow crust rocks (e.g., sedimentary rocks); (4) Basaltic magma; and (5) High-Mg, hydrous hybrid melt derived from the reaction between serpentinite and basalt magma.

Author Contributions: The paper was conceived and written by V.S., with contribution and review of the co-authors. A.C and A.P. performed LA-ICPMS analyses in the sample and elaborated the results according to most advanced protocols. All authors contributed to the evaluation and discussion of the data.

Conflicts of Interest: The authors declare no conflict of interest.

References

1. Newhall, C.; Self, S. The Volcanic Explosivity Index (VEI): An Estimate of Explosive Magnitude for Historical Volcanism. *J. Geophys. Res.* **1982**, *87*, 1231–1238. [CrossRef]
2. Giordano, D.; Russel, J.K.; Dingwell, D.B. Viscosity of magmatic liquids: A model. *Earth. Planet. Sci. Lett.* **2008**, *271*, 123–134. [CrossRef]
3. Schmincke, H.-U. *Volcanism*; Springer: Berlin, Germany, 1998; p. 324, ISBN 3-540-43650-2.
4. Coltelli, M.; Del Carlo, P.; Vezzoli, L. Stratigraphic constraints for explosive activity in the past 100 ka at Etna Volcano, Italy. *Int. J. Earth. Sci.* **2000**, *89*, 65–677. [CrossRef]
5. Del Carlo, P.; Pompilio, M. The relationship between volatile content and the eruptive style of basaltic magma: The Etna case. *Ann. Geophys.* **2004**, *47*, 1423–1432.
6. Kamenetsky, V.S.; Pompilio, M.; Métrich, N.; Sobolev, A.V.; Kuzmin, D.V.; Thomas, R. Arrival of extremely volatile-rich high-Mg magmas changes explosivity of Mount Etna. *Geology* **2007**, *35*, 255–258. [CrossRef]
7. Swanson, D.A.; Rose, T.R.; Mucek, A.E.; Garcia, M.O.; Fiske, R.S.; Mastin, L.G. Cycles of explosive and effusive eruptions at Kīlauea Volcano Hawai'i. *Geology* **2014**, *7*, 631–634. [CrossRef]

8.   Amore, C.; Giuffrida, E.; Scribano, V.; Lowenstern, J.B.; Müller, W. Emplacement and textural analysis of some present-daypyroclastic deposits of Mt Etna, Sicily. *Boll. Soc. Geol. Ital.* **1987**, *106*, 785–791.

9.   Coltelli, M.; Del Carlo, P.; Pompilio, M.; Vezzoli, L. Explosive eruption of a picrite: The 3930 BP subplinian eruption of Etna volcano, Italy. *Geophys. Res. Lett.* **2005**, *32*, L23307. [CrossRef]

10.   Patterson, M.; Francis, D.; McCandless, T. Kimberlites: Magmas or mixtures? *Lithos* **2009**, *112*, 191–200. [CrossRef]

11.   White, J.; Ross, P.-S. Maar-diatreme volcanoes: A review. *J. Volcanol. Geotherm. Res.* **2011**, *201*, 1–29. [CrossRef]

12.   Graettinger, A.H.; Valentine, G.A.; Sonder, I.; Ross, P.-S.; White, J.D.L.; Taddeucci, J. Maar-diatreme geometry and deposits: Subsurface blast experiments with variable explosion depth. *Geochem. Geophys. Geosyst.* **2014**, *15*, 740–764. [CrossRef]

13.   Anderson, A.T. CO_2 and the eruptibility of picrite and komatiite. *Lithos* **1995**, *34*, 19–25. [CrossRef]

14.   Saal, A.E.; Hauri, E.H.; Langmuir, C.H.; Perfit, M.R. Vapor undersaturation in primitive mid-ocean ridge basalts and the volatile content of Earth's upper mantle. *Nature* **2002**, *419*, 451–455. [CrossRef] [PubMed]

15.   Hauri, E.H.; Gaetani, G.A.; Green, T.H. Partitioning of water during melting of the Earth's upper mantle at H_2O-undersaturated conditions. *Earth Planet. Sci. Lett.* **2000**, *248*, 715–734. [CrossRef]

16.   Scribano, V.; Carbone, S.; Manuella, F.C. Diatreme eruption probably related to explosive interaction of rising magma with serpentinite diapirs in the shallow crust (Carlentini Formation Hyblean area Sicily): A xenolith perspective. *Epitome* **2007**, *2*, 130–131.

17.   Manuella, F.C.; Carbone, S.; Ferlito, C.; Hovland, M. Magma–serpentinite interaction as the origin of diatremes: A case study from the Hyblean Plateau (southeastern Sicily). *Int. J. Earth Sci.* **2016**, *105*, 1371–1385. [CrossRef]

18.   Viccaro, M.; Scribano, V.; Cristofolini, R.; Ottolini, L.; Manuella, F.C. Primary origin of some trachytoid magmas: Inferences from naturally quenched glasses in hydrothermally metasomatized gabbroic xenoliths (Hyblean area Sicily). *Lithos* **2009**, *113*, 659–672. [CrossRef]

19.   Herzberg, C. Depth and degree of melting of komatiite. *J. Geophys. Res.* **1992**, *97*, 4521–4540. [CrossRef]

20.   Herzberg, C.; O'Hara, M.J. Plume-associated ultramafic magmas of Phanerozoic age. *J. Petrol.* **2002**, *43*, 1857–1883. [CrossRef]

21.   Gudfinnsson, G.H.; Presnall, D.C. Continuous gradations among primary carbonatitic kimberlitic melilitic basaltic picritic and komatiitic melts in equilibrium with garnet lherzolite at 3–8 GPa. *J. Petrol.* **2005**, *46*, 1645–1659. [CrossRef]

22.   Elkins-Tanton, L.T.; Draper, D.S.; Agee, C.B.; Jewell, J.; Thorpe, A.; Hess, P.C. The last lavas erupted during the main phase of the Siberian flood volcanic province: Results from experimental petrology. *Contrib. Mineral. Petrol.* **2007**, *153*, 191–209. [CrossRef]

23.   Herzberg, C.; Asimov, P.D.; Arndt, N.; Niu, Y.L.; Lesher, C.M.; Fitton, J.G.; Cheadle, M.J.; Saunders, A.D. Temperatures in ambient mantle and plumes: Constraints from basalts picrites and komatiites. *Geochem. Geophys. Geosys.* **2007**, *8*, Q02006. [CrossRef]

24.   Lentini, F.; Carbone, S.; Catalano, S. Main structural domains of the central Mediterranean region and their Neogene tectonic evolution. *Boll. Geofis. Teor. Appl.* **1994**, *36*, 141–144.

25.   Rocchi, S.; Longaretti, G.; Salvadori, M. Subsurface Mesozoic and Cenozoic magmatism in southeastern Sicily: Distribution volume and geochemistry of magmas. *Acta Vulcanol.* **1998**, *10*, 395–408.

26.   De Rosa, R.; Mazzuoli, R.; Scribano, V.; Trua, T. Nuovi dati petrologici sulle Vulcaniti dei Monti Iblei (Sicilia sud-orientale): Implicazioni genetiche e geotettoniche. *Miner. Petrogr. Acta* **1991**, *34*, 133–151.

27.   Tonarini, S.; D'Orazio, M.; Armenti, P.; Innocenti, F.; Scribano, V. Geochemical features of Eastern Sicily lithosphere as probed by Hyblean xenoliths and lavas. *Eur. J. Mineral.* **1996**, *8*, 1153–1173. [CrossRef]

28.   Schmincke, H.U.; Behncke, B.; Grasso, M.; Raffi, S. Evolution of the northwestern Iblean Mountains Sicily: Uplift Plicocene/ Pleistocene sea–level changes paleoenvironment and volcanism. *Geol. Rundsch.* **1997**, *86*, 637–669. [CrossRef]

29.   Beccaluva, L.; Siena, F.; Coltorti, M.; Digrande, A.; Lo Giudice, A.; Macciotta, G.; Tassinari, R.; Vaccaro, C. Nephelinitic to tholeiitic magma generation in a transtensional tectonic setting: An integrated model for the Iblean vulcanism, Sicily. *J. Petrol.* **1998**, *39*, 1547–1576. [CrossRef]

30. Trua, T.; Esperança, S.; Mazzuoli, R. The evolution of the lithospheric mantle along the N African Plate: Geochemical and isotopical evidence from the tholeiitic and alkaline volcanic rocks of the Hyblean Plateau Italy. *Contrib. Mineral. Petrol.* **1998**, *131*, 307–322. [CrossRef]
31. Correale, A.; Martelli, M.; Paonita, A.; Scribano, V.; Arienzo, I. A combined study of noble gases trace elements and Sr–Nd isotopes for alkaline and tholeiitic lava from the Hyblean Plateau (Italy). *Lithos* **2018**, *314–315*, 59–70. [CrossRef]
32. Suiting, I.; Schmincke, H.U. Internal vs external forcing in shallow marine diatreme formation: A case study from the Iblean Mountains (SE-Sicily Central Mediterranean). *J. Volcanol. Geotherm. Res.* **2009**, *186*, 361–378. [CrossRef]
33. Scribano, V.; Sapienza, G.T.; Braga, R.; Morten, L. Gabbroic xenoliths in tuff-breccia pipes from the Hyblean Plateau: Insights into the nature and composition of the lower crust underneath Southeastern Sicily, Italy. *Mineral. Petrol.* **2006**, *86*, 63–88. [CrossRef]
34. Scribano, V.; Ioppolo, S.; Censi, P. Chlorite/smectite-alkali feldspar metasomatic xenoliths from Hyblean Miocenic diatremes (Sicily, Italy): Evidence for early interaction between hydrothermal brines and ultramafic magmatic rocks at crustal levels. *Ofioliti* **2006**, *31*, 161–171.
35. Manuella, F.C.; Scribano, V.; Carbone, S.; Brancato, A. The Hyblean xenolith suite (Sicily): An unexpected legacy of the Ionian–Tethys realm. *Int. J. Earth Sci.* **2015**, *104*, 1317–1336. [CrossRef]
36. Beccaluva, L.; Bianchini, G.; Coltorti, M.; Natali, C. Comment on Manuella et al "The Hyblean xenolith suite (Sicily): An unexpected legacy of the Ionian–Tethys realm". *Int. J. Earth Sci.* **2015**, *104*, 1679–1684. [CrossRef]
37. Manuella, F.C.; Scribano, V.; Carbone, S.; Brancato, A. Reply to "Comment on Manuella et al 'The Hyblean xenolith suite (Sicily): An unexpected legacy of the Ionian–Tethys realm' by Beccaluva et al 2015". *Int. J. Earth Sci.* **2015**, *104*, 1685–1691. [CrossRef]
38. Ben Avraham, Z.; Boccaletti, M.; Cello, G.; Grasso, M.; Lentini, F.; Torelli, L.; Tortorici, L. Principali domini strutturali originatisi dalla collisione neogenico–quaternaria nel Mediterraneo centrale. *Mem. Soc. Geol. Ital.* **1990**, *45*, 453–462.
39. Finetti, I.; Lentini, F.; Carbone, S.; Del Ben, A.; Di Stefano, A.; Forlin, E.; Guarnieri, P.; Pipan, M.; Prizzon, A. Geological outline of Sicily and lithospheric tectono-dynamics of its Tyrrhenian margin from new CROP seismic data. In *CROP Project: Seismic Exploration of the Central Mediterranean and Italy*; Finetti, I.R., Ed.; Elsevier: Amsterdam, The Netherlands, 2005; Volume 15, pp. 319–376.
40. Dellong, D.; Klingelhoefer, F.; Kopp, H.; Graindorge, D.; Margheriti, L.; Gutscher, M.A. Crustal Structure of the Ionian Basin and Eastern Sicily Margin: Results from a Wide-Angle Seismic Survey. *J. Geophys. Res. Solid Earth* **2018**, *123*, 2090–2114. [CrossRef]
41. Hyndman, R.D.; Peacock, S.M. Serpentinization of the forearc mantle. *Earth Planet. Sci. Lett.* **2003**, *212*, 417–432. [CrossRef]
42. Giampiccolo, E.; Brancato, A.; Manuella, F.C.; Carbone, S.; Gresta, S.; Scribano, V. New evidence for the serpentinization of the Palaeozoic basement of southeastern Sicily from joint 3-D seismic velocity and attenuation tomography. *Geophys. J. Int.* **2017**, *211*, 1375–1395. [CrossRef]
43. Musumeci, C.; Scarfì, L.; Palano, M.; Patanè, D. Foreland segmentation along an active convergent margin: New constraints in southeastern Sicily (Italy) from seismic and geodetic observations. *Tectonophysics* **2014**, *630*, 137–149. [CrossRef]
44. Burollet, F.P. Structures and tectonics of Tunisia. *Tectonophysics* **1991**, *195*, 359–369. [CrossRef]
45. Thibault, N.; Galbrun, B.; Gardin, S.; Minoletti, F.; Le Callonnec, L. The end-Cretaceous in the southwestern Tethys (Elles Tunisia): Orbital calibration of paleoenvironmental events before the mass extinction. *Int. J. Earth Sci.* **2016**, *105*, 771–795. [CrossRef]
46. Manuella, F.C.; Brancato, A.; Carbone, S.; Gresta, S. A crustal- upper mantle model for southeastern Sicily (Italy) from the integration of petrologic and geophysical data. *J. Geodyn.* **2013**, *66*, 92–102. [CrossRef]
47. D'Alessandro, A.; Mangano, G.; D'Anna, G.; Scudero, S. Evidence for serpentinization of the Ionian upper mantle from simultaneous inversion of P- and S-wave arrival times. *J. Geodyn.* **2016**, *102*, 115–120. [CrossRef]
48. Polonia, A.; Torelli, L.; Gasperini, L.; Cocchi, L.; Muccini, F.; Bonatti, E.; Hensen, C.; Schmidt, M.; Romano, S.; Artoni, A.; et al. Lower plate serpentinite diapirism in the Calabrian Arc subduction complex. *Nat. Commun.* **2017**, *8*, 2172. [CrossRef] [PubMed]

49. De Guidi, G.; Imposa, S.; Scudero, S.; Palano, M. New evidence for Late Quaternary deformation of the substratum of Mt Etna volcano (Sicily Italy): Clues indicate active crustal doming. *Bull. Volcanol.* **2014**, *76*, 816–829. [CrossRef]

50. Manuella, F.C.; Ottolini, L.; Carbone, S.; Scavo, L. Metasomatizing effects of serpentinization-related hydrothermal fluids in abyssal peridotites: New contributions from Hyblean peridotite xenoliths (southeastern Sicily). *Lithos* **2016**, *264*, 405–421. [CrossRef]

51. Manuella, F.C.; Della Ventura, G.; Galdenzi, F.; Carbone, S. Sr-rich aragonite veins in Hyblean serpentinized peridotite xenoliths (Sicily, Italy): Evidence for abyssal-type carbonate metasomatism. *Lithos* **2019**, *326–327*, 200–212. [CrossRef]

52. Scribano, V. Natural partial melting of pyroxenite nodules and megacrysts from Sicily: A preliminary report. *Period Miner.* **1988**, *57*, 65–72.

53. Scribano, V.; Viccaro, M.; Cristofolini, R.; Ottolini, L. Metasomatic events recorded in ultramafic xenoliths from the Hyblean area (Southeastern Sicily Italy). *Mineral. Petrol.* **2009**, *95*, 235–250. [CrossRef]

54. Perinelli, C.; Sapienza, G.T.; Armienti, P.; Morten, L. Metasomatism of the upper mantle beneath the Hyblean Plateau (Sicily): Evidence from pyroxenes and glass in peridotite xenoliths. *Geol. Soc.* **2008**, *293*, 197–221. [CrossRef]

55. Frost, R.B.; Beard, J.S. On silica activity and serpentinization. *J. Petrol.* **2007**, *48*, 1351–1368. [CrossRef]

56. Evans, B.W. The serpentinite multisystem revisited: Chrysotile is metastable. *Int. Geol. Rev.* **2004**, *46*, 479–506. [CrossRef]

57. Palandri, J.L.; Reed, M.H. Geochemical models of metasomatism in ultramafic systems: Serpentinization rodingitization and sea floor carbonate chimney precipitation. *Geochim. Cosmochim. Acta* **2004**, *68*, 1115–1133. [CrossRef]

58. Blackman, D.K.; Karson, J.A.; Kelley, D.S.; Cann, J.R.; Früh-Green, G.L.; Gee, J.S.; Hurst, S.D.; John, B.E.; Morgan, J.; Nooner, S.L.; et al. Geology of the Atlantis Massif (Mid-Atlantic Ridge 30°N): Implications for the evolution of an ultramafic oceanic core complex. *Mar. Geophys. Res.* **2004**, *23*, 443–469. [CrossRef]

59. Silantyev, S.A.; Bortnikov, N.S.; Shatagin, K.N.; Bel'tenev, V.E.; Kononkova, N.N.; Bychkova, Y.V.; Krasnova, E.A. Petrogenetic conditions at at 18°–20°N MAR: Interaction between hydrothermal and magmatic systems. *Petrology* **2016**, *24*, 336–366. [CrossRef]

60. Le Bas, M.J. IUGS reclassification of the high-Mg and picritic volcanic rocks. *J. Petrol.* **2000**, *41*, 1467–1470. [CrossRef]

61. Kerr, A.C.; Arndt, N.T. A note on the IUGS reclassification of the high-Mg and picritic volcanic rocks. *J. Petrol.* **2001**, *42*, 2169–2171. [CrossRef]

62. Vasil'ev, Yu.R.; Gora, M.P. Meimechite–picrite associations in Siberia, Primorye, and Kamchatka (comparative analysis and petrogenesis). *Russ. Geol. Geophys.* **2014**, *55*, 959–970. [CrossRef]

63. Clague, D.A.; Weber, W.S.; Dixon, J.E. Picritic glasses from Hawaii. *Nature* **1991**, *353*, 553–555. [CrossRef]

64. Winchester, J.A.; Floyd, P.A. Geochemical discrimination of different magma series and their differentiation products using immobile elements. *Chem. Geol.* **1977**, *20*, 325–343. [CrossRef]

65. Pearce, J.A. Geochemical fingerprint of oceanic basalts with applications to ophiolite classification and the search for Archean oceanic crust. *Lithos* **2008**, *100*, 14–48. [CrossRef]

66. Fitton, J. The OIB paradox. *Geol. Soc. Am.* **2007**, *430*, 387–412. [CrossRef]

67. Arndt, N.; Lehnert, K.; Vasil'ev, Y. Meimechites: Highly magnesian lithosphere-contaminated alkaline magmas from deep subcontinental mantle. *Lithos* **1995**, *34*, 41–59. [CrossRef]

68. Heinonen, J.S.; Luttinen, A.V. Jurassic dikes of Vestfjella, western Dronning Maud Land, Antarctica: Geochemical tracing of ferropicrite sources. *Lithos* **2008**, *105*, 347–364. [CrossRef]

69. Clague, D.A.; Moore, J.G.; Dixon, J.E.; Friesen, W.B. Petrology of submarine lavas from Kilauea' Puna Ridge, Hawaii. *J. Petrol.* **1995**, *36*, 299–349. [CrossRef]

70. Natland, J.H. Capture of mantle helium by growing olivine phenocrysts in picritic basalts from the Juan Fernandez Islands, SE Pacific. *J. Petrol.* **2003**, *44*, 421–456. [CrossRef]

71. Kogarko, L.N.; Ryabchikov, I.D. Geochemical evidence for meimechite magma generation in the subcontinental lithosphere of Polar Siberia. *J. Asian Earth Sci.* **2000**, *18*, 195–203. [CrossRef]

72. Milidragovic, D.; Chapman, J.B.; Bichlmaier, S.; Canil, D.; Zagorevskic, A. H_2O-driven generation of picritic melts in the Middle to Late Triassic Stuhini arc of the Stikine terrane, British Columbia, Canada. *Earth Planet. Sci. Lett.* **2016**, *454*, 65–77. [CrossRef]

73. Sobolev, A.V.; Sobolev, S.V.; Kuzmin, D.V.; Malitch, K.N.; Petrunin, A.G. Siberian meimechites: Origin and relation to flood basalts and kimberlites. *Russ. Geol. Geophys.* **2009**, *50*, 999–1033. [CrossRef]

74. Gale, A.; Dalton, C.A.; Langmuir, C.H.; Su, Y.; Schilling, J.G. The mean composition of ocean ridge basalts. *Geochem. Geophys. Geosyst.* **2013**, *14*, 489–518. [CrossRef]

75. Alt, J.C.; Shanks, W.C. Serpentinization of abyssal peridotites from the MARK area Mid-Atlantic Ridge: Sulfur geochemistry and reaction modeling. *Geochim. Cosmochim. Acta* **2003**, *67*, 641–653. [CrossRef]

76. Frost, R.B. On the stability of sulphides oxides and native metals in serpentinite. *J. Petrol.* **1985**, *26*, 31–63. [CrossRef]

77. Yoder, H.S., Jr.; Tilley, C. Origin of basalt magmas: Experimental study of natural and synthetic rock systems. *J. Petrol.* **1962**, *3*, 342–532. [CrossRef]

78. Wright, T.L.; Okamura, R.T. *Cooling and Crystallization of Tholeiitic Basalt, 1965 Makaopuhi Lava Lake, Hawaii*; Geological Survey Professional Paper 1004; United States Government Printing Office: Washington, DC, USA, 1977; pp. 1–47.

79. Rudge, J.F.; Kelemen, P.B.; Spiegelman, M. A simple model of reaction induced cracking applied to serpentinization, carbonation of peridotite. *Earth Planet. Sci. Lett.* **2010**, *291*, 215–227. [CrossRef]

80. Wohletz, K.; Zimanowski, B.; BuÃàttner, R. Magma–water interactions. In *Modeling Volcanic Processes: The Physics and Mathematics of Volcanism*; Sarah, A., Fagents, S.A., Gregg, T.K.P., Lopes, R.M.C., Eds.; Cambridge University Press: Cambridge, UK, 2012; pp. 231–257.

81. Viti, C. Serpentine minerals discrimination by thermal analysis. *Am. Mineral.* **2010**, *95*, 631–638. [CrossRef]

82. Seipold, U.; Schilling, F.R. Heat transport in serpentinites. *Tectonophysics* **2003**, *370*, 147–162. [CrossRef]

83. Peltonen, P. Metamorphic olivine in picritic metavolcanics from Southern Finland. *Bull. Geol. Soc. Finl.* **1990**, *62*, 99–114. [CrossRef]

84. Gualtieri, A.F.; Giacobbe, C.; Viti, C. The dehydroxylation of serpentine group minerals. *Am. Mineral.* **2012**, *97*, 666–680. [CrossRef]

85. Dunbar, R.C.; Petrie, S. Magnesium Monocationic Complexes: A Theoretical Study of Metal Ion Binding Energies and Gas-Phase Association Kinetics. *J. Phys. Chem.* **2005**, *109*, 1411–1419. [CrossRef] [PubMed]

86. Rodriguez-Cruz, S.E.; Jockusch, R.A.; Williams, E.R. Hydration energies and structures of alkaline earth metal ions, $M^{2+}(H_2O)n$, n = 5–7, M = Mg, Ca, Sr, and Ba. *J. Am. Chem. Soc.* **1999**, *121*, 8898–8906. [CrossRef]

87. Mysen, B.O.; Boettcher, A.L. Melting of a hydrous mantle. I. Phase relations of natural peridotite at high pressures and temperatures with controlled activities of water, carbon dioxide and hydrogen. *J. Petrol.* **1975**, *33*, 347–375. [CrossRef]

88. Ferlito, C.; Coltorti, M.; Lanzafame, G.; Giacomoni, P. The volatile flushing triggers eruptions at open conduit volcanoes: Evidence from Mount Etna volcano (Italy). *Lithos* **2014**, *184*, 447–455. [CrossRef]

89. Zimanowski, B.; Böttner, R. Dynamic mingling of magma and liquefied sediments. *J. Volcanol. Geotherm. Res.* **2002**, *114*, 37–44. [CrossRef]

90. De Rosa, R.; Donato, P.; Ventura, G. Fractal analysis of mingled/mixed magmas: An example from the Upper Pollara eruption (Salina Island southern Tyrrhenian Sea Italy). *Lithos* **2002**, *65*, 299–311. [CrossRef]

91. Morgavi, D.; Perugini, D.; De Campos, C.; Ertel-Ingrisch, W.; Dingwell, D. Time evolution of chemical exchanges during mixing of rhyolitic and basaltic melts. *Contrib. Mineral. Petrol.* **2013**, *166*, 615–638. [CrossRef]

92. Perugini, D.D.; Campos, C.P.; Petrelli, M.; Morgavi, D.; Vetere, F.P.; Dingwel, D.B. Quantifying magma mixing with the Shannon entropy: Application to simulations and experiments. *Lithos* **2015**, *236*, 299–310. [CrossRef]

93. Correale, A.; Paonita, A.; Martelli, M.; Rizzo, A.; Rotolo, S.G.; Corsaro, R.A.; Di Renzo, V. A two component mantle source feeding Mt Etna magmatism: Insights from the geochemistry of primitive magmas. *Lithos* **2014**, *184*, 243–258. [CrossRef]

94. Arndt, N.T.; Nisbet, E.G. What is a komatiite? In *Komatiites*; Arndt, N.T., Nisbet, E.G., Eds.; Allen & Unwin: London, UK, 1989; pp. 19–28.

95. Agee, C.B.; Walker, D. Static compression and olivine flotation in ultrabasic silicate liquid. *J. Geophys. Res.* **1988**, *93*, 3437–3449. [CrossRef]

96. Cox, K.G. A model for flood basalt volcanism. *J. Petrol.* **1980**, *21*, 629–650. [CrossRef]

97. Falloon, T.J.; Green, D.H.; Danushevsky, L. Crystallization temperatures of tholeiite parental liquids: Implications for the existence of thermally driven mantle plumes. In *Plates Plumes and Planetary Processes*; Foulger, G.R., Jurdy, D.M., Eds.; Geological Society of America: Boulder, CO, USA; pp. 235–260.

98. Hammouda, T.; Laporte, D. Ultrafast mantle impregnation by carbonatite melts. *Geology* **2000**, *28*, 283–285. [CrossRef]

99. Nixon, P.H. *Mantle Xenoliths*; John Willey & Sons: London, UK, 1987; p. 640.

100. Punturo, R.; Scribano, S. Dati geochimici e petrografici su xenoliti di clinopirossenite a grana ultragrossa e websteriti nelle vulcanoclastiti mioceniche dell'alta Valle Guffari (Monti Iblei, Sicilia). *Miner. Petrogr. Acta* **1997**, *40*, 95–116.

101. Thorpe, A.K. Evidence from Experimental Petrology for Olivine Addition in Meimechite Magma Generation. Ph.D. Thesis, Department of Geological Sciences, Brown University, Providence, RI, USA, 2004. Available online: http://www.geog.ucsb.edu/~{}akthorpe/documents/Andrew_K_Thorpe_Honors_Thesis.pdf (accessed on 6 June 2018).

102. Boudier, F.; Nicolas, A.; Ildefonse, B. Magma chambers in the Oman Ophiolite: Fed from the top and the bottom. *Earth Planet. Sci. Lett.* **1996**, *144*, 239–250. [CrossRef]

103. Scribano, V.; Carbone, S.; Manuella, F.C. Tracking the Serpentinite Feet of the Mediterranean Salt Giant. *Geosciences* **2018**, *8*, 352. [CrossRef]